Satellite observations of clouds and precipitation processes and their interactions

Graeme Stephens, Kentaroh Suzuki, John Haynes, Matthew Lebsock, Duane Waliser, Todd Ellis, Angela Benedetti, Hui Su, Jay Mace and Zhengzhao Luo

Department of Atmospheric Science, Colorado State University
Fort Collins, CO USA
stephens@atmos.colostate.edu

1. Introduction

The capabilities for observing clouds, precipitation and processes connected to condensed water in the atmosphere by satellites that presently orbit the Earth is unprecedented in the history of space-borne Earth observations. The so-called A-Train of satellites (Stephens et al., 2002), in particular, represents entirely new observations of key cloud and precipitation processes in a way more advanced that ever before. These new observations are a unique source of information for evaluating the moist physics parameterizations in models with benefits that are expected to lead to greatly improved and more realistic representations of these important atmospheric processes.

This paper outlines a collection of the new findings from the A-Train observing system, particularly those that that bear directly on the problem of cloud and convection parameterization.

2. The capabilities of the A-Train

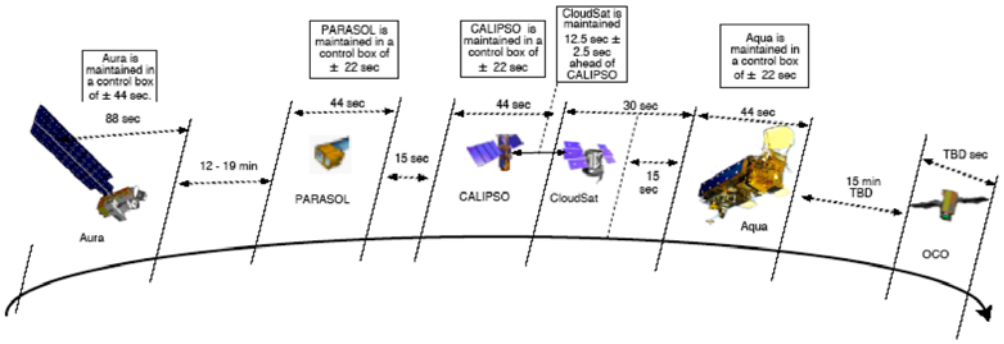

Figure 1: The Afternoon constellation (A-Train) showing in detail the control boxes and the position of each member prior to December, 2007. The position of both CloudSat with respect to CALIPSO and Aura with respect to the constellation has been slightly changed from this formation (Stephens et al., 2008).

The A-Train currently consists of 5 spacecraft flying in the formation shown in Fig. 1. Three other spacecraft are to join this formation in the coming years, including the OCO observatory, the GLORY mission and possibly the GCOM-W mission of JAXA. The orbits of the constellation are sun-synchronous with a mean equatorial altitude of 705 km and an inclination of 98.2 degrees. This orbit is 'frozen' such that there are no long-term period changes in the orbital elements resulting in an orbit of constant size and shape, thus reducing altitude variations over any spot on the Earth and improves the repeatability of scientific

observations. These different spacecraft provide measurements of the atmosphere with very different types of information contained in them. As illustrated throughout this paper, these different perspectives are highlighted in terms of cloud and precipitation processes.

The formation of the constellation is coordinated to ensure safety of the constellation. It is maintained via the notion of a 'control box' which is a theoretical construct centered at a reference position on a satellite's drag-free orbit with dimensions defined by an allowable along-track movement relative to the box's center (the reference position, refer to Fig. 1). CloudSat is unique among all members, as its control box lies within the CALIPSO control box and is much more tightly maintained at 5 seconds in size. This stems from the requirement to place footprints of the radar and lidar within 2 km of each other (across track) 50% of the time. Thus CloudSat is the only spacecraft in the formation that must make frequent, routine adjustments in its orbit location (called circulation orbits) to maintain the desired spatial overlap of footprints with respect to CALIPSO while maintaining a close proximity with Aqua. As of January 2008, CloudSat has conducted over sixty maneuvers to maintain this formation in comparison to just 4 manouvers by the other spacecraft. This provides the capability of matching the CloudSat radar observation to the CALIPSO lidar observations thereby offering a unique view of particles suspended in the atmosphere. Analysis indicates that the overlap requirement has been substantially exceeded with overlap of the CloudSat radar (CPR) and lidar footprints occurring more than 90% of the time. In this way CloudSat has demonstrated that precision formation flying is a practical and viable observing strategy that can be exploited in the design of future Earth observing systems. Figure 2 demonstrates the incredible ability of the formation flying providing the means to overlay the observations of the lidar and radar in a precise way serving as the basis of the 2B-GEOPROF-lidar product of CloudSat (e.g. Mace et al., 2008).

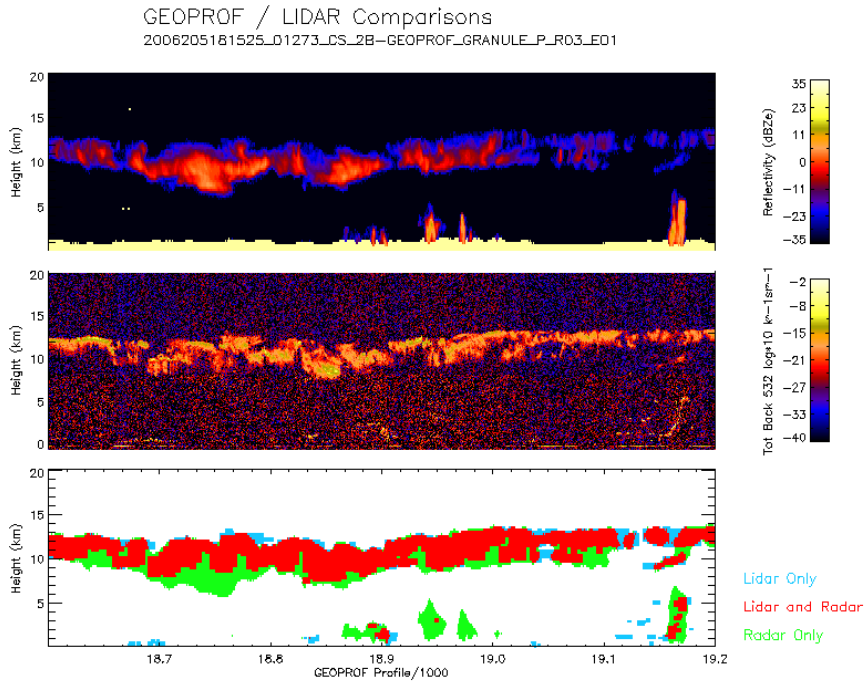

Figure 2: CloudSat radar (upper) and CALIPSO lidar (middle) profiles of cirrus and the overlay of the two (lower) as provided in the 2B-GEOPROF-lidar product (refer to Mace et al., 2008 for more details).

3. Global cloudiness

The combination of A-Train lidar and radar observations provides the most comprehensive depiction of global cloudiness yet produced. These combined observations reveal a global hydrometeor coverage of

approximately 76% and a small annual cycle of about by 3% varying smoothly between a maximum peaking in October 2006 and a minimum in March 2007 (Fig. 3).

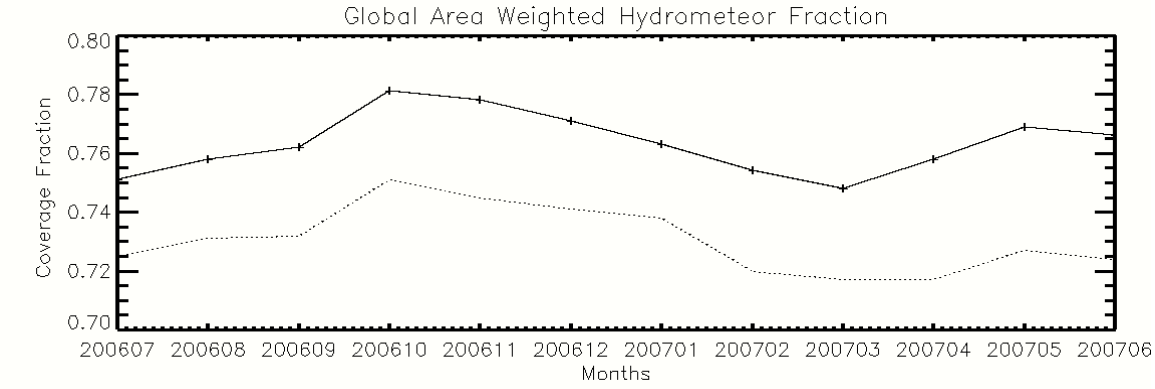

Figure 3. Monthly hydrometeor coverage fraction derived from the merged Cloudsat-Calipso data (solid) and from the MODIS cloud mask sampled along the Cloudsat-Calipso Track (Mace et al., 2008).

3.1. Zonal average structures

The kind of cloud cover information presented above has been available from satellite observations for some time but the new observations now offer a completely new dimensional view of clouds exposing their vertical structure, statistics of cloud overlap and other information not previously available. Figure 4 (taken Mace et al., 2008) highlights this new capability showing the zonal average of the vertical distribution of hydrometers derived from the combination of lidar and radar observations provided by the Cloudsat 2B-Geoprof-lidar product. From this figure one observes the well-known features of the general circulation including clouds associated with the ITCZ and the extensive cirrus over the tropical oceans.

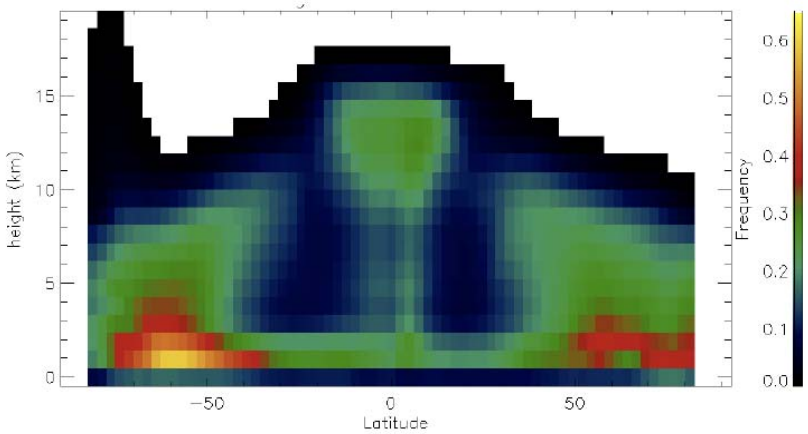

Figure 4: Zonally averaged vertical occurrence in 2° latitude bins from the merged 2B-Geoprof-lidar product. The averaging period is from July, 2006 through June 2007 (from Mace et al., 2008).

Evaluation of models using these new observations is now underway and these evaluations should lead to improved parameterizations of cloud processes. A number of such model evaluation activities are being developed around the use of the CPR simulator (e.g. Haynes et al., 2007; Bodas-Salcedo et al., 2008) and an example of such a study is shown in Fig. 5 where the frequency of occurrence refers to those clouds with reflectivities greater than -30 dBZ. Although the pattern of the vertical distribution of hydrometeors simulated by the model is broadly similar to the observations, there are notable differences. Models produce fewer hydrometeors in mid-latitudes below 5 km, and the presence of hydrometeors in the lower levels of

tropical deep convection is clearly underestimated compared to the observations. The underestimation at lower levels switches to overestimation above 8 km suggesting that convection detrains too much moisture at high levels, therefore producing too much cloud at these levels in the tropics. Deep convective clouds also do not reach levels as high as observed, with a very small hydrometeor fraction above 14 km.

Area weighted joint height-reflectivity histograms are given in Figs 5c and 5d. There seems to be linear relationship between maximum reflectivity and height, with increasing maximum reflectivity with decreasing height, with an approximate slope of Low levels, below 3 km, how a slightly bimodal distribution, with a peak around -25 dBZ, and a second maximum near 5 dBZ. The transition between these two modes is smooth in the observations (low cloud - drizzle - rainfall) but not in the model which reveals a entirely different picture. At lower levels, the model seems to operate in two regimes, one with non-precipitating cloud (reflectivities ~ -30 dBZ), and the other for precipitating cloud (reflectivities ~ 5 dBZ). In the mid and high levels, the model exhibits a much smaller range of reflectivities, with the majority of points clustered around a much tighter height-reflectivity relationship than observed. This points to the parameterization of ice microphysics that is to narrow in its variability.

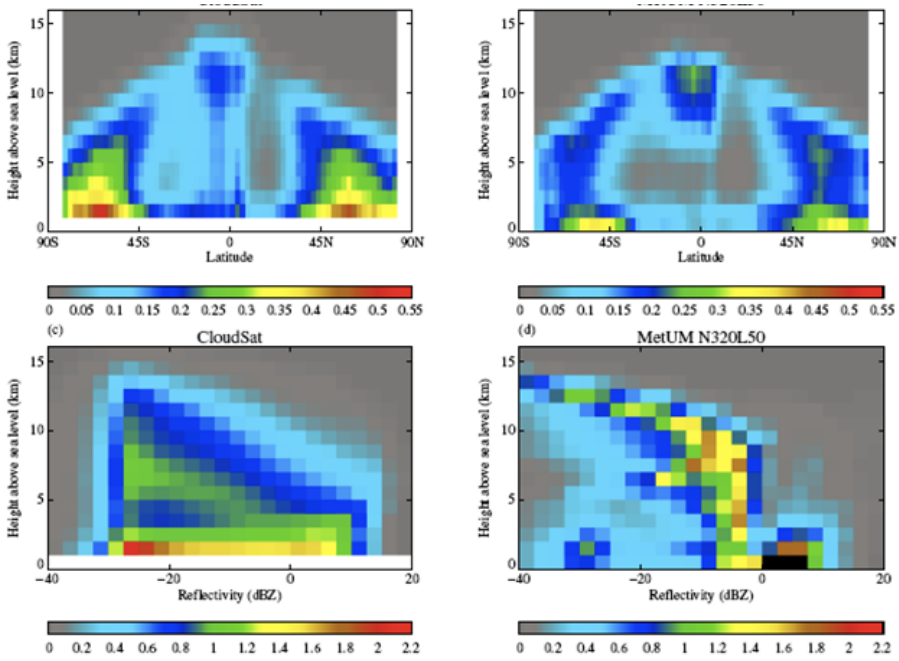

Figure 5: Comparison of DJF 2006 statistics for the whole globe: (a) zonal mean cross-section of hydrometeor occurrence as observed by CloudSat (left upper) , and (b) simulated by the MetUM model (right upper0; (c) joint height-reflectivity frequency of occurrence as observed by CloudSat (left lower) , and (d) simulated by the MetUM global forecast model (right lower; from Bodas-Salcedo et al., 2008).

3.2. Multilayer characteristics

These new measurements are also well suited for identifying the presence of multiple cloud layers. Figure 6a shows the global distribution of the occurrence of multiple cloud layers where layers defined require a hydrometeor-free distance of 4 range bins (approximately 1 km) between the top of a lower layer and the base of the next highest layer. Globally, the occurrence of multiple layers is 24% compared to Wang et al. (2000) who report a global multi-layer occurrence of approximately 40%. Figure 6 shows that the occurrence of multiple layers is a strong function of latitude and geography with multiple layer occurrences over the tropical oceans exceeding 60% of all cloudy profiles such as in regions of the western Pacific and elsewhere in the ITCZ. Haynes et al (2008) similarly note that multiple layering is also ubiquitous in tropical precipitating systems, occurring more than 50% of the time precipitation is detected. Multiple layers tend to

occur more often over the storm tracks of the north Pacific than over the Southern Ocean. The marine stratus regions and subtropical latitudes in general where free tropospheric subsidence is strong (i.e. the descending branch of the Hadley Cells) are regions of minimum multiple layer occurrence.

The predominant co-occurrence of multiple hydrometeor layers is essentially dominated by low based layers occurring with high-based layers over oceanic regions equatorward of 45° in each hemisphere (Figure 6c and also noted in Haynes and Stephens, 2007). Poleward of these latitudes, occurrence of multiple layers is predominantly low-based with mid-based clouds while multiple low layers are observed in the high latitudes of the Southern Ocean. The occurrence of mid level layers with high-based layers tends to be a continental phenomenon in addition to in the ITCZ of the western Pacific and Indian Oceans. Multiple high-based layers tend to occur primarily over the tropical oceans and over the subtropical continents. It is difficult to rectify these results with the seminal cloud climatology of Warren et al. (1985).

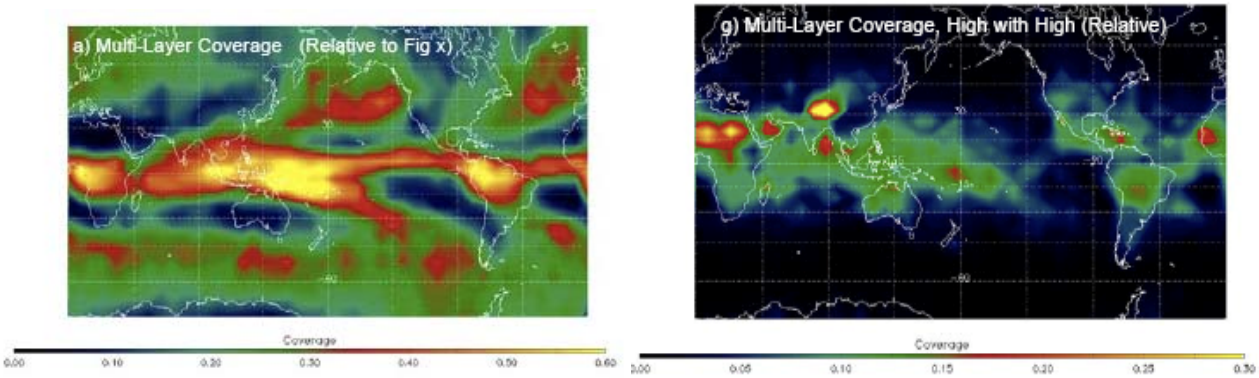

Figure 6: Multiple layer coverage. a) (top left) The coverage of multiple layers from the merged Cloudsat-CALIPSO data set where the total number of multiple layer profiles (defined as a profile with a 1 km hydrometeor-free space between range volumes that contain hydrometeors) are normalized by the total number of profiles. b) (top right) as in a) except that high-based with high-based is shown c) (bottom left) as in a) except that low-based with high-based (layer base > 6 km) is shown. d) as in a) except that mid-based with high based is shown. The averaging period is from July, 2006 through June 2007 in 6x8 degree latitude-longitude averaging regions, (adapted from Mace et al., 2008).

3.3. Tropical thin cirrus

The joint detection characteristics of both the CloudSat radar and CALIPSO lidar also offer a unique perspective on the properties of tropical thin cirrus clouds. These measurement characteristics were used to study tropical thin cirrus observed between 20ºN and 20ºS in the study of Haladay and Stephens, 2008. They considered two types of thin cirrus, thin ice cloud category (TIC-1) of cirrus that are detected by the lidar but not the radar and the TIC-2 cirrus category as detected by both sensors. Lidar-based estimates of optical depth suggest the TIC-1 optical depths range between 0.02 to 0.3, thereby expressing the sensitivity of the CloudSat radar in terms of visible optical depth. The ice water path (IWP) of TIC-1 clouds is also estimated to be between .5 and 4 g/m2. The radiative properties of the TIC-1 clouds are also deduced from CloudSat flux data products at the top, bottom and within the atmosphere. The influence of these clouds on the instantaneous reflected solar fluxes is determined to be less than 2 Wm^{-2}. The effects of TIC-1 clouds on the instantaneous out-going longwave fluxes is estimated to be ~20 Wm-2 and the impact of these TIC-1 clouds on the tropics-wide average of the infrared heating is ~4 Wm^{-2}.

Tropical TIC-1 cirrus clouds between 20ºN and 20ºS are observed to be high, optically thin, and have an approximate cloud cover in the defined region of 25% (Fig. 7). Almost a third of this occurrence is in the form of single layers of cloudiness without any clouds below. Approximately 40% of the occurrence is with

one other cloud layer below either thicker layers of cirrus 1-2 km below or with shallow clouds in the boundary layer.

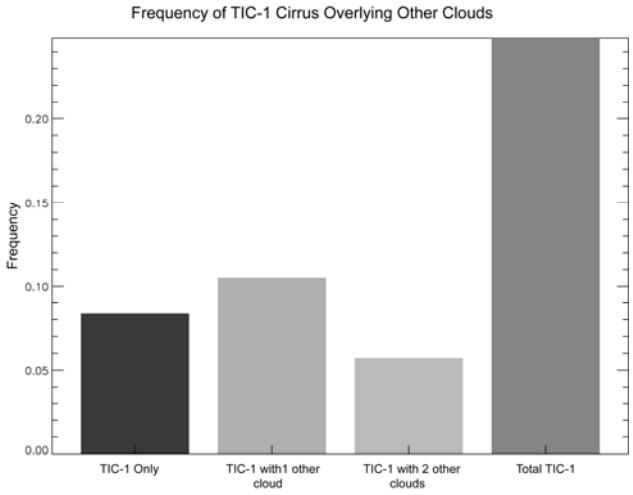

Figure 7: The frequency with which TIC-1 cirrus occurs with other clouds in the same atmospheric column. The total occurrence of TIC-1 is shown on the far right bar for reference, which is approximately 25% of the time throughout the entire Tropics (20º N/S). Of that 25%, only just over 8% of the time are those TIC-1 cirrus clouds occurring without other clouds present (~1/3 of all TIC-1 cirrus). Over 10% of the time they occur above 1 other cloud and over 5% they occur with 2 or more other clouds in the same atmospheric column.

These TIC-1 clouds also exhibit a marked seasonal variation, especially away from the equator, that appears consistent with the climatological shifts in convection through the annual cycle. This seasonal cycle is highlighted in Fig. 8 showing occurrences averaged over the entire region of study and between 20ºN and the Equator. These seasonal cycles are presented for approximately 2 years of CloudSat and CALIPSO data. The seasonal variation of the Northern Hemisphere is smaller than the Southern Hemisphere tropical averages where the former variation peaks around August and has a minimum in DJF. On the other hand, the large variation in the tropical Southern Hemisphere varies between 20% in the JJA season and near 40% in DJF. The seasonal cycles are more marked for regions further away from the equator (not shown).

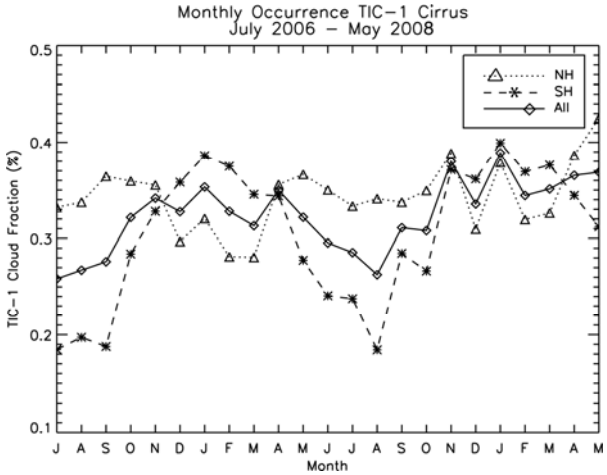

Figure 8: Monthly averages of frequency of occurrence of TIC-1 cirrus clouds from July 2006 to May 2008. Plotted are northern hemisphere tropical averages (20ºN to Equator) as the dashed line, southern hemisphere tropical averages (Equator to 20ºS) as the dotted line, and a tropical average (20ºN to 20ºS) as the black solid line (from Haladay and Stephens, 2008).

4. Cloud and precipitation Properties

4.1. Warm Cloud properties

The combination of CloudSat observations matched to MODIS and AMSR-E provides for unique global characterization of the properties of warm clouds and offers a way of relating these properties to other characteristics of clouds. Figure 9 shows the joint distribution of the MODIS-derived cloud water path *W* and effective radius re for oceanic, warm clouds where the matched CPR precipitation classification (described below) has been applied to these data. The results show how warm precipitating clouds tend to be both wetter (larger W) and composed of larger particles (i.e. larger re) than non-precipitating clouds.

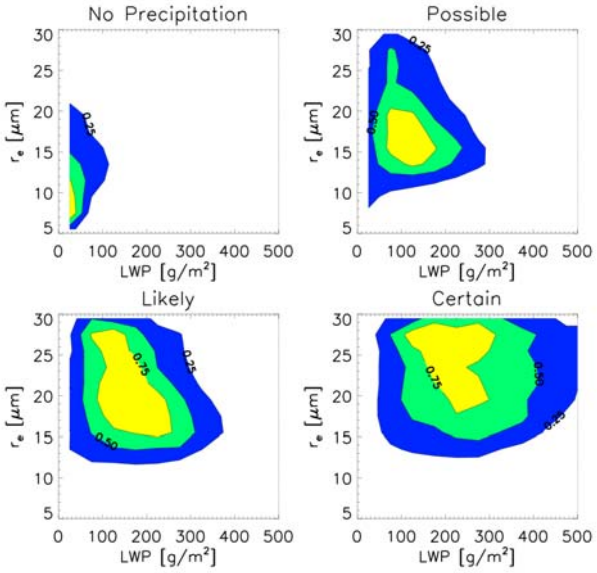

Figure 9: The joint distributions of cloud liquid water path and effective radius classified into the four precipitation categories derived from matched CloudSat CPR observations (from Stephens et al., 2008).

These results are further expanded upon in Fig 10 showing the liquid water path (from MODIS) as a function of cloud depth (from the CloudSat radar) contrasted against the LWP predicted from adiabatic assumptions. The probability of precipitation (POP) is also shown as a function of cloud depth revealing how the likelihood of precipitation increases significantly with increasing cloud depth.

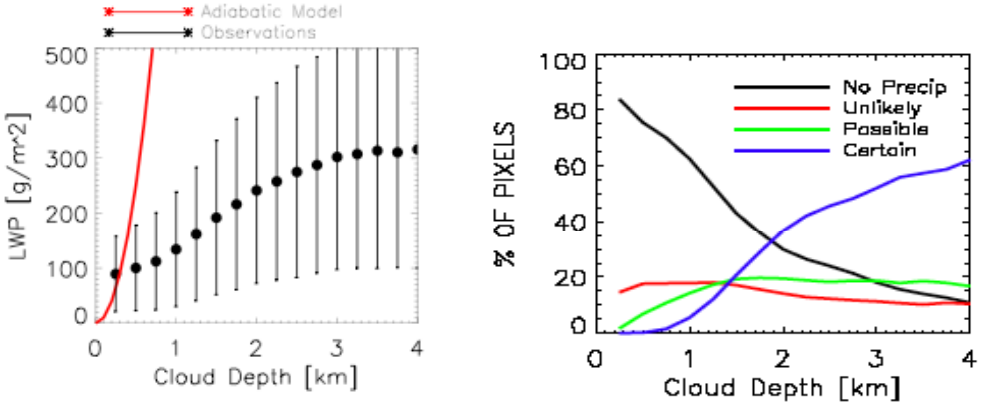

Figure 10(a) right: the cloud LWP derived from AMSR-E as a function of cloud depth derived from CloudSat observations. The LWP calculated assuming adiabatic ascent is provided for reference. (b) left: the percentage of individual CPR column profiles that contain the four different classes of rain as a function of cloud depth (adapted from Stephens et al., 2008).

4.2. Cold cloud properties

The CloudSat 2B-CWC-RO data product provides an estimate of ice water content (Austin et al., 2008). This is an important product as it provides the most comprehensive estimate of the amount of ice in the global atmosphere. The global and annual averaged ice water path (IWP) derived from this product is highlighted in Fig 11a. These products include both precipitating and non-precipitating ice and this, in itself adds ambiguity when comparing to global models. The IWP is shown for each of the cloud types defined by the 2B-CLDCLASS product of CloudSat, and the data are further grouped into 'convective' (cumulus and deep convection) and 'non-convective' (all other types) cloud categories as way of separating clouds with non precipitating ice from clouds with precipitating ice. The uncertainties shown correspond to the estimated, systematic uncertainties derived from analysis as described in more detail in Austin et al. (2008).

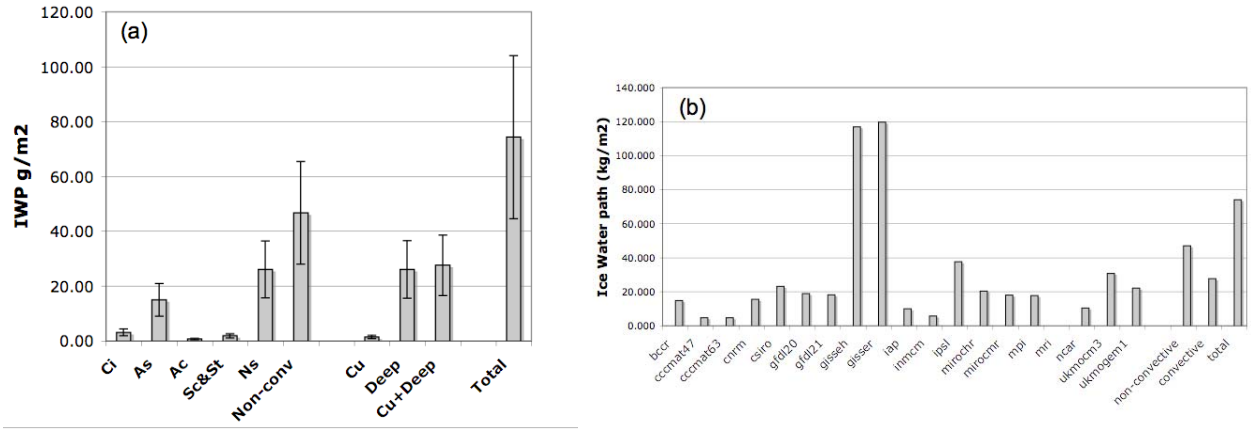

Figure 11 (a) Global mean ice water path calculated from Release 4 (R04) of the CloudSat 2B-CWC-RO product over the period 2006-12-01 to 2007-11-30. Ice water path is assigned to cloud types using the 2B-CLDCLASS product. 'Convective' cloud refers to the sum of 2B-CLDCLASS cumulus and deep convection types; 'non-convective' includes the remaining types. Error bars indicate the estimated systematic uncertainties. (b) The global mean ice water path derived from 19 IPCC climate models from the 1970-1994 period of the 20th century GCM simulations contributed to the IPCC 4th Assessment Report (20c3m scenario) compared to the CloudSat observations of non-convective, convective and total repeated from (a) (from Stephens et al., 2008).

The non-convective IWP, the convective IWP and the sum of the two are compared in Fig. 11b to the global and annually averaged IWP derived from several coupled-climate models where the model data are taken from the 1970- 1994 period of the 20th century GCM simulations contributed to the IPCC 4th Assessment Report. Any conclusions drawn from this direct comparison between model and observation should viewed with some caution given the way models segregate clouds into large-scale and convective types and then segregate ice into precipitating ice and non-precipitation ice. Since most convective schemes used by models do not include ice specifically, it is tempting to consider the non-convective ice IWP of CloudSat as a closer proxy to the modeled ice. However, most convective schemes contain some form of detrained ice indirectly, and thus some of the observed convective ice content should also be included in the comparison. Despite these ambiguities, it appears from Fig. 11b that the values of IWPs of most models lie significantly below observed values especially if we suppose that the appropriate observed ice path for comparison lies somewhere between the CloudSat non-convective ice and total ice amounts shown.

Figure 12 illustrates CloudSat's estimate of annual mean IWC in the form of zonal averages of vertically-resolved values of IWC compared to equivalent distributions from the various models indicated. While the results of Figs 11 and 12 indicate the potential value of CloudSat IWC and total IWP data for model validation the model data are not necessarily in a form optimal for comparison to observations as noted. Waliser et al. (2008) address this topic using a more judicious sub-setting of the CloudSat data based on

additional flags and information in the retrieval products [Stephens et al., 2008]. For example, Fig. 13 shows CloudSat IWC values filtered in three different ways, taking only cases that are flagged as having no precipitation (NP) at the ground, those cases classified as non-convective (NC) clouds, and the combination of both of these criteria (NP & NC). For example, the NP case includes all IWC = 0 (i.e. clear) and only the IWC > 0 cases that are non-precipitating at the surface. For interpretation, it is useful to start with the most stringently filtered case, i.e. NP & NC. In this case, the IWC is considerably lower than the total IWC shown in Fig. 12. In some regions, the reduction in IWC is well over 50% through the exclusion of the cases that exhibit precipitation at the surface and those denoted as convective. Both of these excluded cases would be

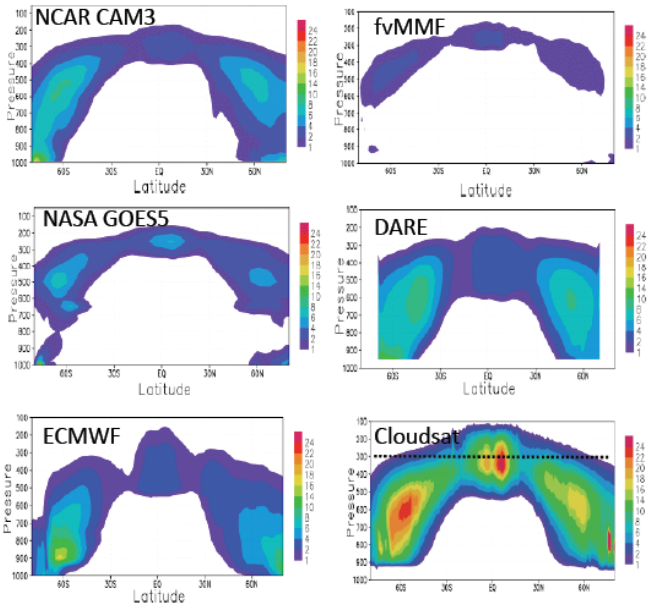

Figure 12: Annual and zonal mean values of cloud ice water content (IWC; mg m-3) from NCAR CAM3 (upper left; 1979-1999), NASA GEOS5 (middle left; 01/1999-12/2002), ECMWF R30 analysis (lower left; 08/2005-07/2006), fvMMF (upper right, 07/98 & 01/99), and DARE GCM (middle right; 1998) and Cloudsat 8/2006-7/2007 (adapted from Waliser et al., 2008)

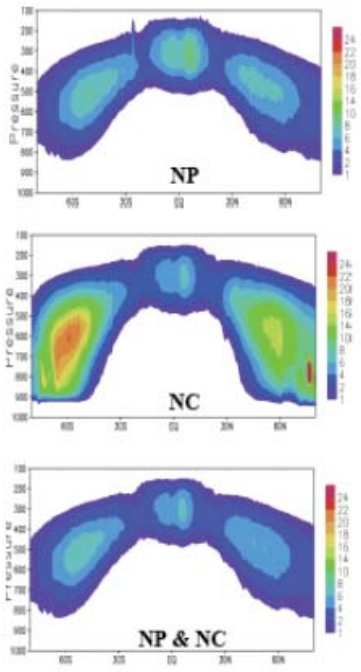

*Figure 13: Annual and zonal mean values of CloudSat IWC (mg m^{-3}) when considering clear cases and those with IWC > 0 but flagged as having no precipitation **at the surface** (NP; upper), cases flagged as non-convective clouds (NC; middle), and those cases that meet both these criteria (NP & NC; lower).*

expected to contain significant amounts of large frozen hydrometeors (e.g., snow, graupel). For the NC case, there is a significant increase in IWC in the mid-latitudes over the NP & NC case. Because the mid-latitude synoptic regime more readily allows for precipitation without convection, the IWC retained is considerably greater – in fact very near the original total in Fig. 12. However, including the precipitating cases does not have a significant impact in the Tropics because most precipitation is associated with convection. This is why all three cases tend to be the same for the tropics, i.e. they retain only about 30% of total cloud ice observed by CloudSat. Interestingly, this fraction of retained ice – referred to as 'floating' cloud ice by Waliser et al. (2008) – is similar to the model total ice of Fig 12.

4.3. Precipitation

The attenuation of the CPR signal as it penetrates the atmosphere arises from a combination of absorption by gases such as O_2 and H_2O, absorption by cloud droplets, and the absorption and scattering by precipitation sized particles. Isolating the two-way path integrated attenuation (PIA) of the entire atmospheric column at the frequency of the CPR provides a very sensitive way of determining the presence of precipitation within the column (Haynes and Stephens, 2007; Haynes et al., 2008). Over ocean surfaces, this PIA can be determined to better than 2dB, based on estimating of the ocean reflectivity under precipitation. The PIA derived in this way provides a very sensitive indication of precipitation with an estimated minimum sensitivity of approximately 0.02-0.05 mm/hr (details given in Haynes et al., 2008).

The frequency of precipitation occurrence over the global oceans from 2006–2007, as calculated from CloudSat radar data, is compared to ship-based (ICOADS) and island-based (GSOD) data. It is shown that the spatial pattern of the precipitation frequency from CloudSat is consistent with previous climatological studies. Comparison to ship-based data reveal that CloudSat results are consistent with ship observations well into the high latitudes and appear to capture the seasonal cycle of precipitation well. A comparison to island data also shows good qualitative agreement, although the spatial scale mismatch complicates the efficacy of such comparisons. Nevertheless, CloudSat is shown to be a viable platform for obtaining quality satellite-based precipitation frequency measurements.

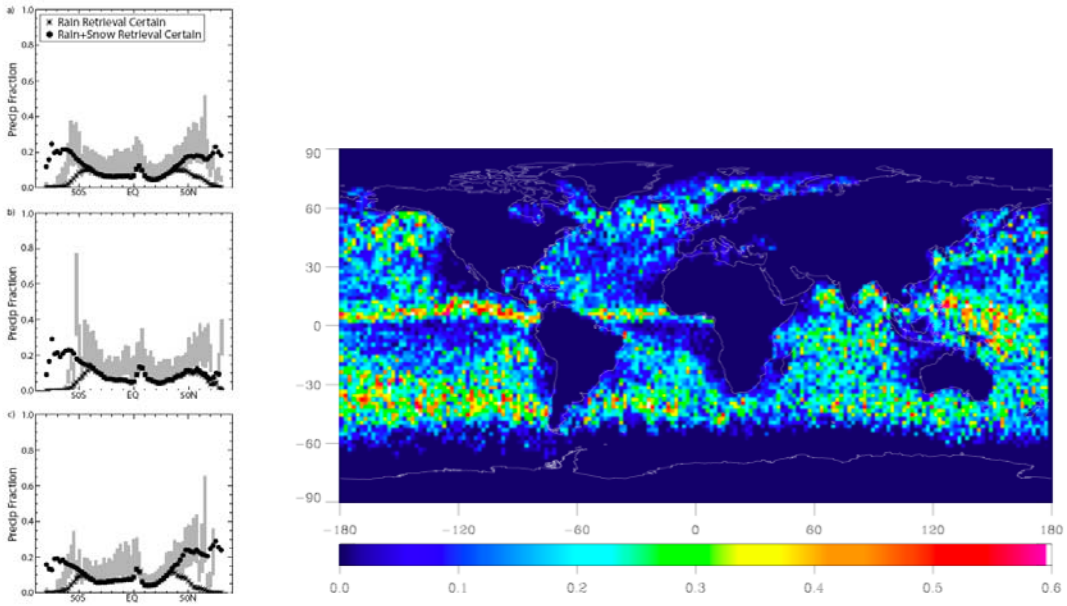

Figure 14: Zonal-mean comparison of precipitation frequency in 2006–2007 as retrieved by CloudSat (circles and stars) versus the range of possible frequencies derived from ship-based weather reports from the ICOADS dataset (grey bars). (a) left-upper depicts the annual mean, while (b) left- middle shows boreal summer (JJA), and (c) left-lower shows austral summer (DJF, adapted from Ellis et al. 2008). (d) the JJA incidence of precipitation as determined by CloudSat up-scaled to 0.5 degrees. The global mean-incidence is 0.13.

Figure 14 presents zonal-mean comparisons of the CloudSat frequency of precipitation occurrence, including certain rain events (asterisks) and certain rain and certain snow events (filled circles) to the ICOADS ship-based reports (grey bars) in the annual mean (Figure 14a), in boreal summer (Figure 14b), and in austral summer (Figure 14c). The meridional patterns of precipitation exhibited in these plots are also consistent with the results of Petty [1995], both seasonally and in the annual mean. The ITCZ is evident in all plots, as are the increased precipitation in the winter hemisphere mid-latitude storms.

Other relevant points include: i) In the annual mean (Figure 14a), the frequency of occurrence of rain and snow when the CloudSat retrieval is certain largely falls within the range of values one would expect based on the ICOADS data between the latitudes of 60°S and 70°N; ii) The retrieval of snow appears to perform very well, as evidenced by the difference between the rain only and combined rain/snow data in the winter hemispheres and because the combined rain/snow data fall within the range provided by ICOADS; iii) The seasonal cycle of precipitation frequency, as illustrated in Figures 14b and 14c, detected by CloudSat is also consistent with that observed from the ICOADS data.

These new results are compared to precipitation incidence derived from the ECMWF operational forecast model (CY33R1) for the JJA 2006 season. Since the native resolution of the satellite data is 1.7km, these data were up-scaled to the model resolution (0.5 degree) via a simple averaging procedure. The results of this up-scaling applied to the PIA-based precipitation incidence for the JJA 2006 season is shown in Fig. 14d. The oceanic mean frequency of occurrence of **liquid** precipitation is 0.13. This is in stark contrast to the results analyzed from the model and shown in Fig 15. Model precipitation was sampled using the minimum precipitation threshold of approximate 0.05mm/hr (at 1.7 km) appropriately up-scaled to determine incidence of precipitation above this threshold. The result presented in Figs 15a-c for total precipitation and precipitation broken down by convective and large-scale respective. The global mean incidence of precipitation derive this way is 0.68.

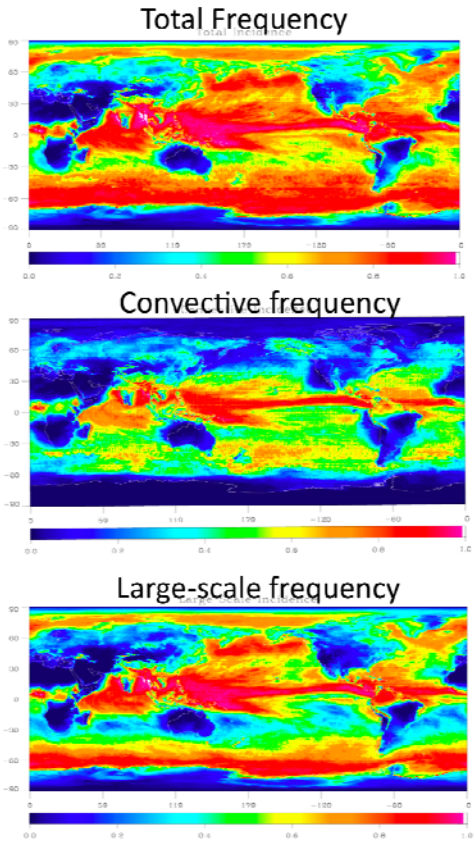

Figure 15: The frequency of occurrence of total, convective and large-scale precipitation that occurs above the CloudSat threshold (refer to text). The colour scale varies linearly from 0 to 1

Another way to examine the character (frequency and intensity) of precipitation is to relate the precipitation falling out of clouds to the properties of clouds themselves. One simple approach is highlighted in Fig. 16 showing the joint distribution of cloud top heights of precipitating clouds and the rain rate (intensity) from these clouds. The results should be viewed as preliminary and show CloudSat data composited at the native resolution of the observations (upper two panels and hence the larger rain rates than that of the model) and the equivalent model results (lower two panels). The results are shown for composites over 20N/S and 50N/S latitudes. There are some important similarities between model and observations in the 20N/S region where the lighter precipitation resembles the distinct bimodal vertical structure previously observed (e.g Haynes and Stephens, 2007). There are, however, clear differences, especially for the composite over the wider latitude range of 50N/S. over these regions, the observations tend to show a pattern of increased rain rate occurring more frequently with lower cloud tops whereas the reverse occurs in models.

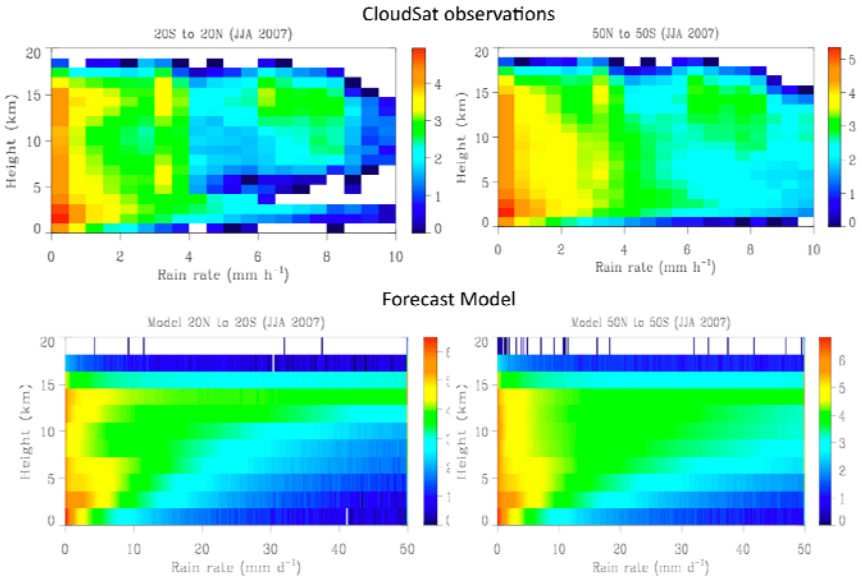

Figure 16: The joint cloud top height –rain rate distributions derived from CloudSat (upper) and the ECMWF forecast model (lower) derived for data over latitudes of 20N/S (left) and 50N/S (right).

5. Processes

5.1. Warm rain

A direct connection between radar reflectivity and the time scale of warm rain formation was recently demonstrated in Stephens and Haynes (2007). That study showed a proportional relation between the time scale of auto-conversion and radar reflectivity for clouds with layer-mean reflectivities less than -15 dBZ. This relation has been further examined in Suzuki and Stephens (2008a) using simulations of a global cloud-resolving model. The parameterizations of auto-conversion and accretion processes in the NICAM model produces a relation between the parameterized time scales for auto-conversion and accretion and radar reflectivity of cloud Zc and rain Zr approximately as Zc^{-1} and $Zr^{-0.5}$ respectively. The overall time scale τ_p for warm rain formation, determined by combined contributions from these processes, is found to relate with total radar reflectivity Ze in the manner that varies with cloud-rain composition. The global statistics from the model reveals that the time scale τ_p closely follows a global relationship $\tau_p \sim Ze^{-0.52}$ (Fig 17a) thus suggesting that the radar reflectivity offers a gross measure of the warm rain time scale. The τ_p-Ze relationship developed is applied to both model-simulated and CloudSat-observed radar reflectivities to compare the time scales of warm rain formation between observation and the model. Comparison of the implied time scale so derived (Fig. 17b) reveals significant differences between the model and CloudSat

observations. These differences suggest that the simulated cloud-rain composition in the model is biased toward larger rain-water contents and smaller content of cloud water compared to reality due to an accelerated cloud-to-rain water conversion in the model. As shown below, this increased rain-water is precipitated out too rapidly from the NICAM model atmosphere.

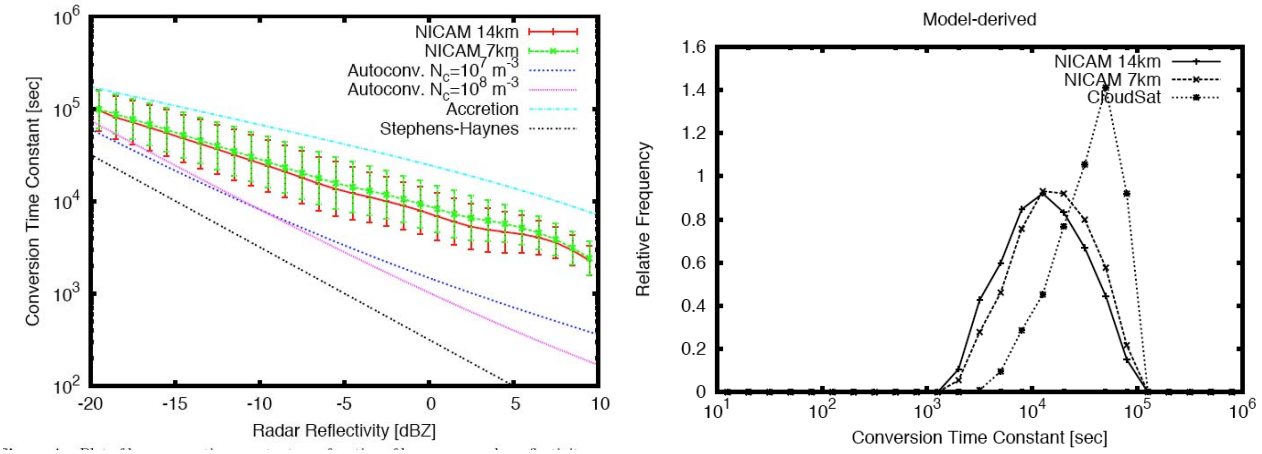

Figure 17a) (left) Plot of layer-mean time constant as a function of layer-mean radar reflectivity b) frequency distributions of warm rain time constant derived from model simulated and CloudSat-observed layer-mean radar reflectivities (adapted from Suzuki and Stephens, 2008a).

Suzuki and Stephens (2008b) introduced a novel connection between the layer-mean radar reflectivity Ze observed by CloudSat and the columnar effective particle radius Re obtained from a combined microwave (AMSR-E)-shortwave (MODIS). The joint relationship between Ze and Re for warm clouds was shown to discriminate cloud droplet growth by condensation from growth by coalescence and identifies the transition between these growth modes. Global statistics for seasonally averaged data (Fig. 18a) reveals that radar reflectivities Ze less than about -10dBZ tend to relate to the effective radius via a sixth-power dependency implying a constant number concentration within the cloud layer for Ze < -10dBZ. For Ze > -10dBZ, Ze depends on Re through a cubic relation implying that liquid water content is conserved under such conditions. These dependencies therefore suggest that the processes of particle growth by condensation and coagulation can be identified in these joint observations and thus these processes can be mapped in the form of a global climatology. These microphysical regimes so identified are found to be consistent with CloudSat-inferred rainfall rate (Figs. 18b and c).

This analysis offers a more probing basis for evaluating model parameterizations of the warm rain process. Shown in Fig. 19 are preliminary results from simulations of the NICAM CRM model (Satoh et al., 2008) and the RAMS CRM model using two different types of parameterizations (a single and double moment microphysics scheme). The radar simulator was coupled to the outputs of these models to derive Ze. These comparisons reveal a model state of warm cloud that has little rain-water in clouds.

Ze from CloudSat as a function of the seasonally averaged columnar effective particle radius Re from combined analysis of AMSR-E and MODIS for JJA 2007 over 60◦S − 60◦N ocean area. Sixth-power dependency for specified values of number concentration N in cm−3 (red lines) and cubic dependency for specified values of mass concentration q in gcm−3 (blue) are also shown for reference. b) and c) (lower) as in a) but separately for light and heavy rainfall regions together with microphysical regimes (adapted from Suzuki and Stephens, 2008b).

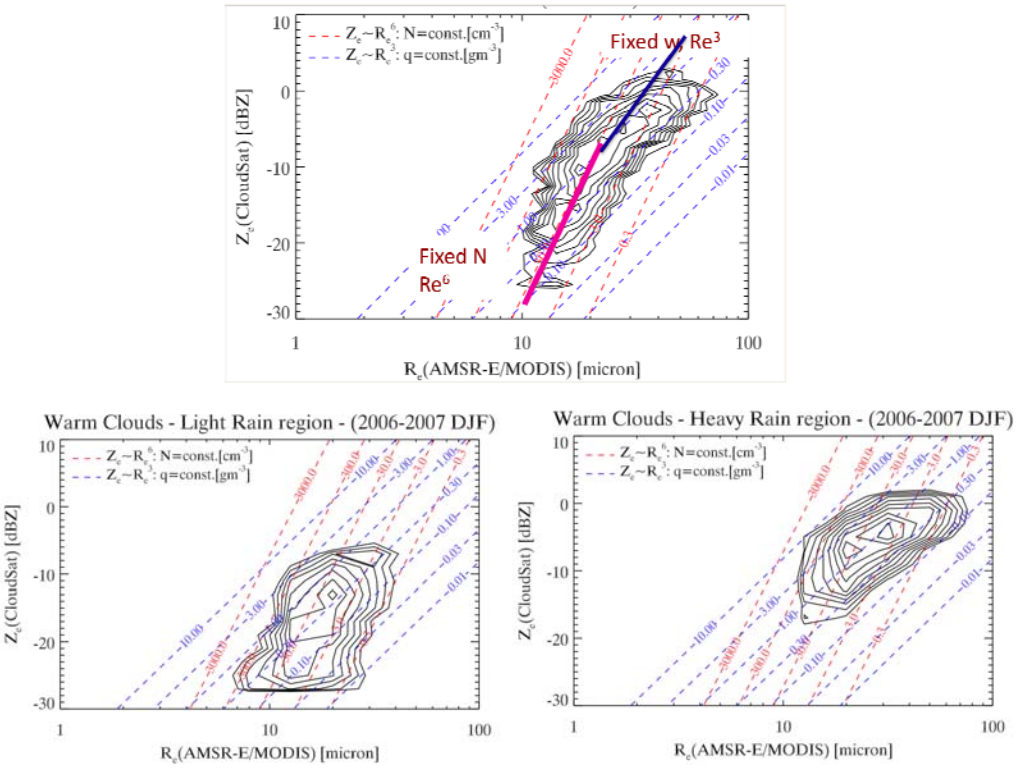

Figure 18a) (upper) Joint probability distribution of the seasonally averaged layer-mean radar reflectivity

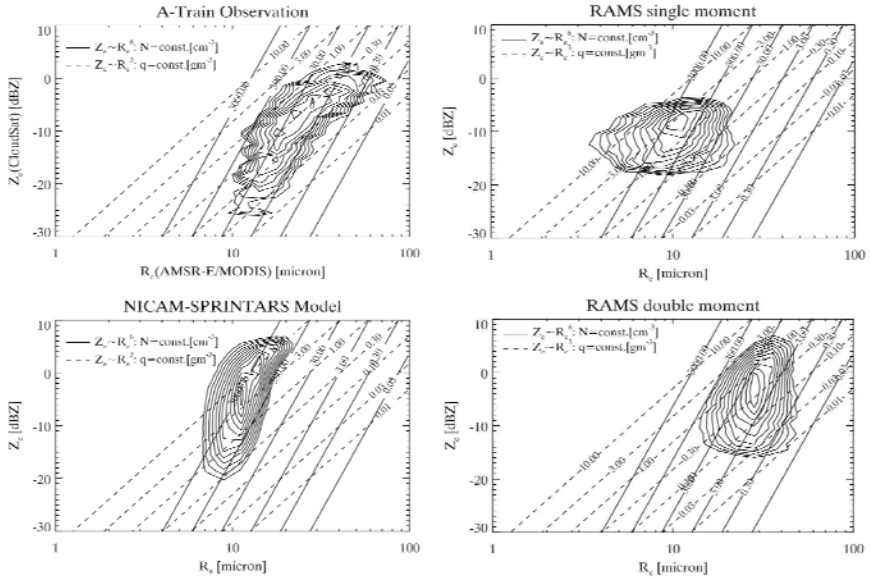

Figure 19: Comparison of the cloud-warm rain transition observed by the A-Train and as represented in two cloud resolving models, NICAM and RAMS

The results highlighted in Figs. 16-19, when considered together, suggest a consistent picture of warm rain and its representation in models- that models make rain too rapidly that falls out too readily with the end result that rain occurs too frequently (and by inference too lightly) compared to the real world. Thus the entire character of model precipitation differs from reality.

5.2. Radiation processes

5.2.1. Cloud Albedo

Changes in cloud albedo figure prominently in a number of important cloud-climate feedback concepts. Cloud albedo changes related to aerosol changes establish the so-called indirect effects of aerosol on climate. Hence, it is of some importance to understand the factors that influence the albedo of clouds and what processes determine them.

The amount of sunlight reflected from clouds is determined largely (although not entirely) by the scaled optical depth of clouds of the form $\tau(1-g)$, where τ is the cloud optical depth and g is the asymmetry parameter. Since the latter quantity is more or less fixed and known a priori for water clouds, then the reflection of sunlight from such clouds can be thought of as governed primarily by τ. Using the relation of Stephens (1978) then

$$\tau = \frac{3}{2\rho}\frac{W}{r_e} \tag{1}$$

where W is the liquid water path of (warm) clouds and r_e is the effective radius. Thus the cloud albedo is function of W and r_e. Satellite measurements of reflected sunlight in selected regions of the solar spectrum, as provided by MODIS for example, provide a way of estimating both τ and re and thus W (Stephens and Kummerow, 2007).

The Twomey effect (Twomey, 1976) appears in (1) via the reduction of re that occurs with enhanced levels of CCN associated with enhanced concentrations of aerosol assuming fixed values of W. Although the idea of the Twomey effect is simple enough, it has proven to be much more difficult than expected to determine if the effect is wide-spread globally and thus has an observable, global consequence on sunlight reflected by the planet. Twomey recognized the important role of meteorology in shaping cloud properties and he argued these effects are more likely to manifest themselves through the cloud water path. The liquid water path of clouds W also varies with changing aerosol amount presumably due to meteorology (e.g Lebsock et al., 2008; Albrecht, 1989) thus making it difficult to isolate aerosol influences uniquely.

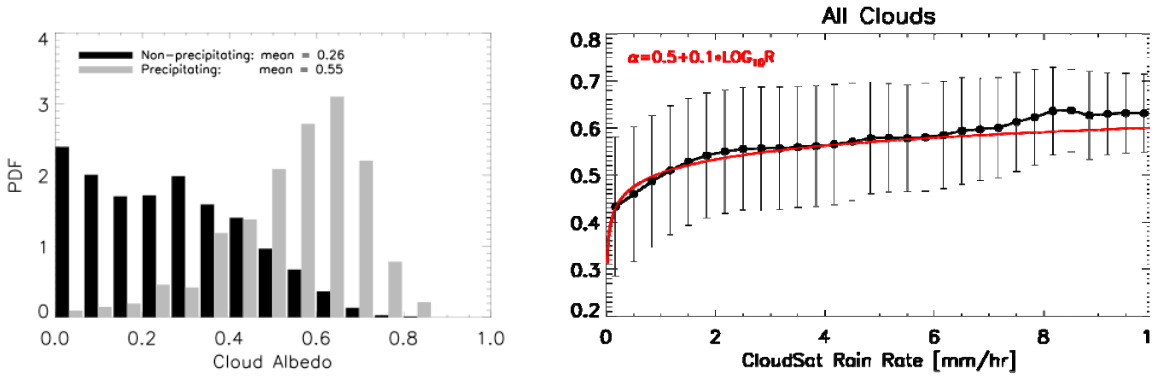

Figure 20 a and b The CERES inferred albedo of precipitating clouds: a) (left) the pdf of the cloud albedo of warm clouds separated into precipitating and non precipitating clouds b) the albedo of all precipitating clouds as observed by CERES and CloudSat as a function of the rain-rate.

The increased water paths of precipitating warm clouds, in contrast to non-precipitating warm clouds, leads to an increased optical depth. The increase in particle size, however, produces a contrary effect that acts to decrease the optical depth and albedo. The combination of these two compensating factors, however, do not

cancel and the optical depths of warm precipitating clouds tend to be significantly larger than those of non-precipitating clouds. As a consequence, these geometrically deeper, wetter precipitating clouds reflect substantially more sunlight than non-precipitating warm clouds (Fig. 20a and b).

5.2.2. Cloud-radiative heating of the atmosphere

The contribution of radiative heating of the atmosphere by clouds is important for many reasons. This heating contribution has remained uncertain yet has a direct influence on the planets hydrological cycle through feedback on convection (e.g. Stephens and Ellis, 2008; Stephens et al., 2008). The vertical structure of clouds largely determines the sign of the net atmospheric heating by clouds and until now it has not been possible to determine this atmospheric heating without gross assumptions about this cloud structure. The CloudSat 2B-FLXHR product incorporates the available observations of cloud vertical structure and derived water contents (L'Ecuyer et al., 2008) in calculations of the vertical profiles of radiative fluxes (and thus heating rates) in cloudy columns. Figure 21 provides the estimated contribution of clouds to the column atmospheric radiative heating (relative to clear skies) for different latitudinal regions and for the entire globe. Figure 21b is an equivalent presentation of the data based on an experimental version of the 2B-FLXHR that adds lidar cloud information. The details of how these undetected (by the CPR) clouds are included in the 2B-FLXHR product are described in L'Ecuyer et al., (2008). Figures 21c and 20d present these cloud radiative heating contributions for three ranges of cloud top height. In general the new observations show clearly how clouds on the global scale radiatively heat the atmosphere by about 8 Wm-2. In general, this heating is dominated by the longwave contribution.

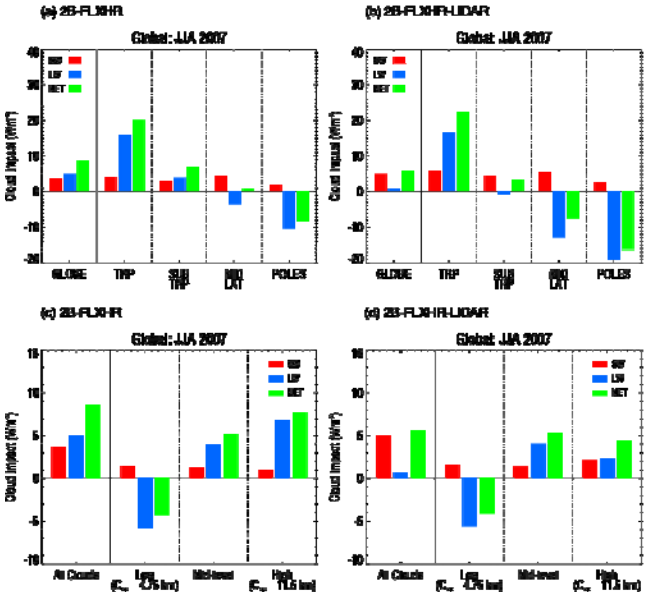

Figure 21: The vertically integrated contribution of clouds to the atmospheric column radiative heating for the JJA season as derived from the CloudSat flux-heating rate products indicated.

5.3. Convection

5.3.1. Deep Penetrating Convection (Luo et al., 2008)

Convection that penetrates the tropical tropopause plays an important role in affecting the heat budget (Sherwood et al. 2003, Kuang and Bretherton 2004) and moisture distributions (Danielsen 1982, Sherwood and Dessler 2000) within the tropical upper troposphere and lower stratosphere. Understanding these important influences requires, in part, ways of observing the tropics-wide distribution and frequency of deep penetrative convection. Here the cloudsat radar data are combined with MODIS data to characterize deep convection. Figure 22 shows typical examples of three modes of penetrative convection classified as follows:

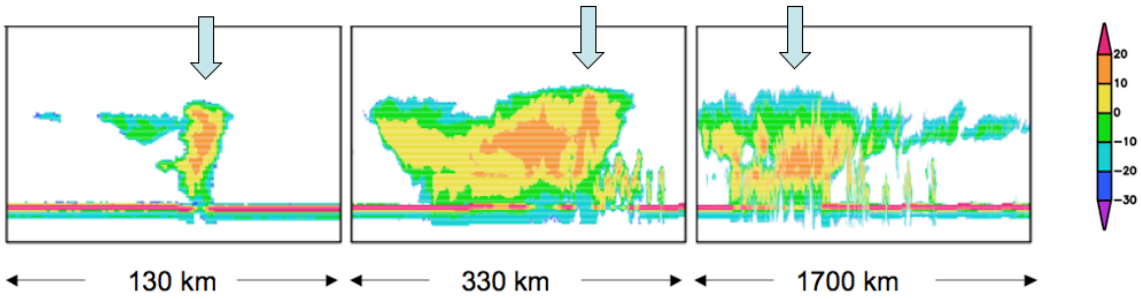

Figure 22: (From left to right) Examples of CL, CH, and WH type tropical penetrating convection. The filled arrows show where the penetration occurs. The color scale is for radar reflectivity in dBZ.

'Cold-low' or CL type convection: Suppose an undiluted convective updraft overshoots the level of neutral buoyancy and continues to rise adiabatically. The cloud top becomes increasingly colder than the surrounding air due to the smaller lapse rate of the environment near the tropopause region (assuming mixing is insignificant). Thus it is possible that the temperature of the convective tower is colder than the cold point temperature of the tropopause (CPT) before it reaches the height of the tropopause. The CL-type convection corresponds to the incipient or growing stage of an overshooting event with little dilution.

'Warm-high' or WH type convection: Convective turrets that penetrate through the CPT and detrain above that level, mix with the warm environment of the lower stratosphere and consequently the cloud top temperature is expected to be warmer than the CPT (Danielsen 1993). Alternatively, it is also possible that as large particles fall to lower levels, the upper portions of these deep clouds might contain mostly small ice crystals and the emission now arises from deeper within the cloud making the cloud appear warmer in the IR brightness temperature compared to the CPT. Either case, we call this 'warm-high' or WH type. The WH type is associated with the mature or dissipating stage.

'Cold-high' or CH type: A third type of penetrating convection is both colder and higher than the local CPT, which we call 'cold-high' or CH type. It is most likely related to newly penetrated convective turret with moderate level of mixing with the environment.

	All	Land	Ocean
CL fraction (out of DC)	0.60%	0.98%	0.41%
CH fraction (out of DC)	0.40%	0.71%	0.31%
WH fraction (out of DC)	0.89%	0.71%	0.93%

Table 1. Occurrence frequencies for different types of penetrating convection (CL, CH and WH) out of the deep convection (DC). The occurrence frequency 0.60% for CL, for example, refers to 0.60% of the DC.

Convection observed by CloudSat is classified into these types by Luo et al (2008) using simultaneous measurement of cloud-top temperature (CTT) provided by MODIS IR data, and independent measurements of cloud-top height (CTH) from cloud radar data with supporting information about the structure below also obtained by the CloudSat radar. A whole year (2007) of CloudSat data are analyzed over 15S-15N. The statistics of this analysis are provided in Table 1. Previous studies have shown that only a small fraction of tropical clouds penetrate to the altitude of the tropopause (e.g., Gettelman et al. 2002, Liu and Zipser 2005, Rossow and Pearl 2007). Between 15S and 15N averaged over a whole year, the occurrence frequency for deep convection (DC) according to the 2B-CLDCLASS product of CloudSat is approximately 3.9%; the

number is slightly larger over land (4.6%) than over ocean (3.7%). Out of this small pool of deep convective profiles, only ~ 1.0% (i.e., 1.0% of the DC) have cloud tops colder than the CPT (the sum of CL and CH in Table 1). This occurrence broadly agrees with the statistics as given in Rossow and Pearl (2007), despite different definitions of deep convection. CloudSat data also show that approximately 1.3% of the DC penetrates beyond the altitude of the CPT. However, the occurrence of cold cloud does not uniquely establish the occurrence of high-reaching convective clouds, and in order to determine the penetrative convection, we break them down into three the types: CL, CH and WH. Table 1 lists the occurrence frequencies of these type: WH type is the most abundant among the three (0.89% of DC), followed by CL type (0.60% of DC), while CH is the least (0.40% of DC). Separated over land and ocean, CL and CH type are a little more than twice as frequently observed over land than over ocean. WH type, on the other hand, is slightly more frequent over ocean.

The echo top height (ETH) for 0 dBZ and 10 dBZ are used to determine to what extent large size particles are lofted by different types of penetrating convection. Table 2 summarizes the statistics of ETH(0 dBZ), ETH(10 dBZ), CTH (which roughly corresponds to the ETH of -28 dBZ), and the distance between the CTH and ETH. Clearly, convective cores for the CL and CH types reach to higher altitudes than do the convective cores in the WH clouds. The contrast is especially striking between CL and WH: despite the fact that WH type convection as a whole rises higher than CL, the corresponding precipitation ETH is noticeably lower. Collocated CALIPSO data were also briefly analyzed for comparison. Because CALIPSO lidar is sensitive to very small particles that are not detected by CloudSat, CTH as defined by CALIPSO is almost always higher than that by CloudSat. Table 2 shows that CTH from CALIPSO is generally within ~ 250 m of that from CloudSat, confirming clouds analyzed here are indeed deep, optically thick convective clouds. Figure 24 schematically summarizes the characteristics of different types of penetrating convection.

	CTH (CloudSat)	CTH (CALIPSO)	Height (0 dBZ)	Distance (top to 0 dBZ)	Height (10 dBZ)	Distance (top to 10 dBZ)
CL	15,752	16,119	14,247	1,505	11,629	4,123
CH	16,668	16,894	15,026	1,642	11,948	4,719
WH	16,521	16,750	14,035	2,486	10,769	5,752

Table 2: Statistics for the internal vertical structure of different types of penetrating convection. The unit is meter.

Independent measurements of CTT and CTH provide direct check on how much dilution convective towers experience. This is accomplished through a comparison of the CTT with the temperature deduced assuming adiabatic, undiluted ascent from the planetary boundary level to the altitude of cloud top (referred to as T-adiabatic). ECMWF equivalent potential temperature at 925 or 1000 hPa, whichever is greater, is used to calculate T-adiabatic, following the procedure in Liu and Zipser (2005). Our calculation shows that the differences between CTT and T-adiabatic, when averaged over a whole year of data, are 1.0 K, 7.7 K and 14 K for CL, CH, and WH types, respectively (Fig. 24). Thus we infer that the CL type comes closest to undiluted adiabatic ascent, whereas CH experiences some moderate level of mixing (with the environment), and WH suffers the most dilution.

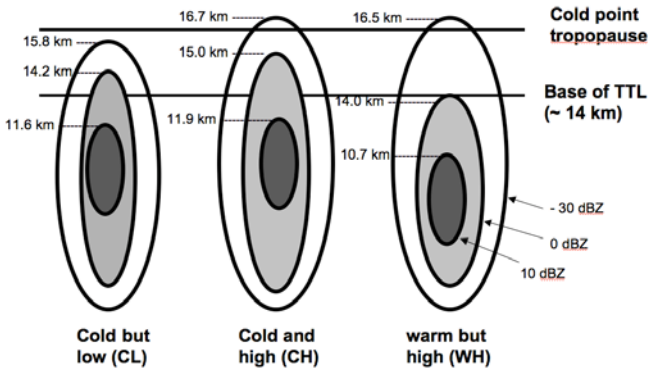

	$\delta T = TB - T(adiabatic)$
CL:	1.0 K
CH:	7.7 K
WH:	14 K

Figure 23: Schematics of the three types of penetrating convection (left) and the derived mean

It is to be expected that these new methods for documenting the statistical nature of convection (e.g. Fig. 24) will provide valuable tools for evaluating the respresentation of convection in global models, either the existing and new parameterizations of convection in global models or the explicit convection in cloud resolving models.

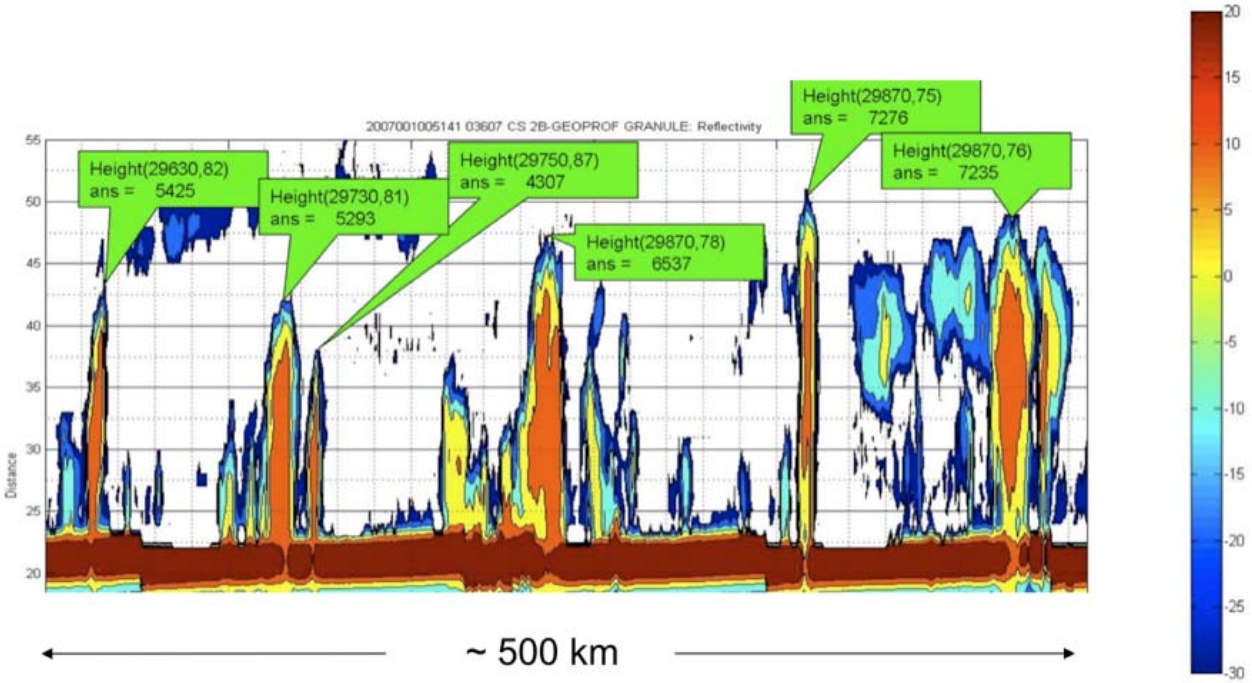

Figure 24: Examples of the height distribution of 'undilute' convective cores where the method of Luo et al. (2008) is applies t other forma of convection.

5.4. Links to the large scale

The CloudSat observed cloud water content (CWC) profiles have been sorted according to a number of large-scale parameters (Su et al., 2008). The large-scale variables (SST, surface convergence derived from NCEP rreanalysis and scatterometer data, SST gradients, TRMM precipitation, moist air, properties from AIRS, AIRS derived CAPE and lower-tropospheric static stability) were interpolated onto CloudSat tracks and the CWC profiles within each bin of a given large-scale variable are averaged. Only tropical oceanic measurements (30°S-30°N) are considered in this binning. Approximately 35 million IWC and LWC profiles were composited in this way for 2007 and over 2 terabytes of data were processed for the one-year data analysis.

Two dominant vertical modes of tropical clouds emerge from the analysis provided in Fig. 25. The deep mode with peak CWCs around 8-10 km is associated with mid-tropospheric ascent, warm SSTs, surface convergence, weak SST gradients, heavy precipitation, moist air, large CAPE and weak lower-tropospheric static stability. The opposite conditions apply to the shallow clouds which have peak CWC (LWC) between 1-2 km. The results are consistent with our existing knowledge for the deep and shallow clouds. An infrequent mode of middle-level clouds also appears. These middle-level clouds usually overlie shallow clouds with surface conditions that are not favorable to deep convection. These clouds may possibly result from the influence of middle-latitude storms as they are associated with cold SST, strong surface divergence, SST gradient, dry air and strong LTS. However, this mechanism is largely ruled out as these features are not eliminated when the binned averages are restricted to 15°S-15°N (figures not shown) suggesting these middle-clouds may be associated with convection initiated at middle-levels. The physical processes that produce these middle-level clouds need to be further studied.

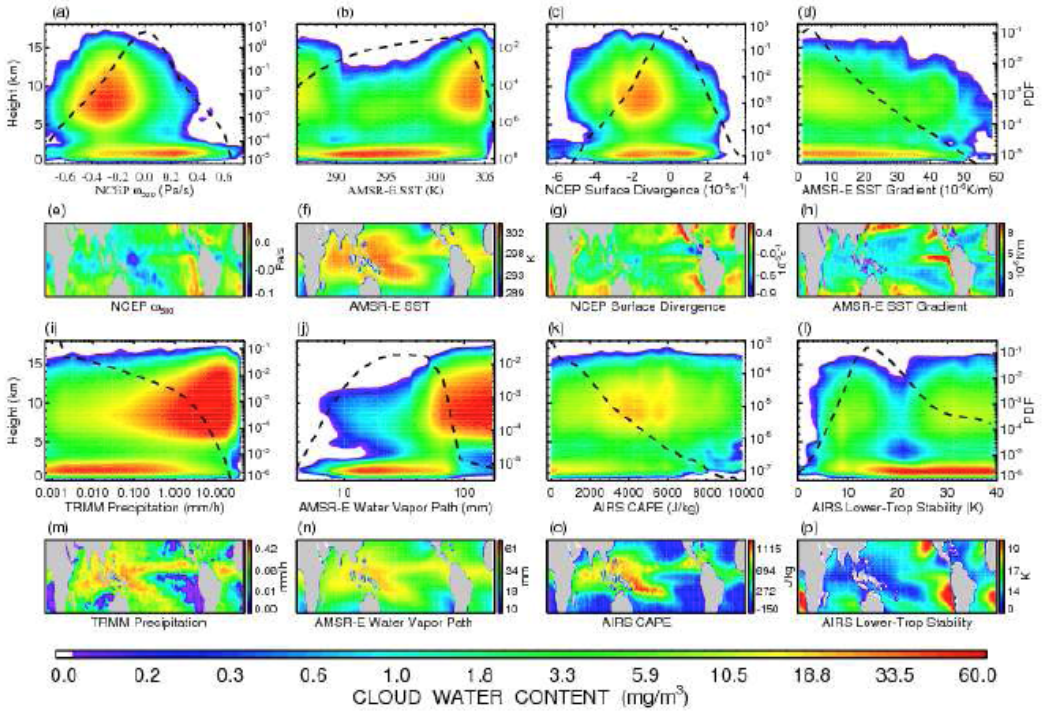

Figure 25:. CWC profiles sorted by various large-scale parameters. The probability density function of each large-scale parameter is plotted in dashed black curve. The map of each large scale parameter is shown below the corresponding binned plot (from Su et al., 2008).

Although the association of cloud structure with large-scale dynamics has been well established, the lack of sorted CWC profiles in large-scale regimes hindered the evaluation of cloud simulations and improvement of cloud parameterizations in climate models [Wyant et al., 2006]. The regime-sorted cloud profiles as presented in Fig 25 and further in Su et al. (2008) can serve as new observational metrics for comparison with models.

6. Summary

The capabilities of satellites that presently orbit the Earth for observing clouds, precipitation and processes connected to condensed water in the atmosphere is unprecedented in the history of space-borne Earth observations. This paper outlines a number of recent studies that exploit the A-Train constellation of satellites (Stephens et al., 2002) to examine the properties of clouds, precipitation and processes that connect

them. The results of a number of these studies are also contrasted to the properties of models with hints at model parameterization. Real advances in the modeling of clouds and precipitation are to be expected through the incorporation of this new knowledge being either directly or indirectly into model parameterizations schemes.

7. References

Albrecht, B., 1989; Aerosol, cloud microphysics, and fractional cloudiness, Science, 245, 1227-1230.

Austin, R A. Heymsfield and G.Stephens, 2008 Retrievals of ice cloud microphysical parameters using the CloudSat millimeter-wave radar and temperature, submitted to J. Geophys. Res.

Bodas-Salcedo,A., M. J. Webb, M. E. Brooks, M. A. Ringer, S. F. Milton, and D. R. Wilson, 2008; Evaluation of cloud systems in the Met Office global forecast model using CloudSat data, submitted to J. Geophys. Res.

Danielsen, E. F. ,1982: A dehydration mechanism for the stratosphere. Geophys. Res. Lett., 9, 605 – 608

Danielsen, E, 1993: In situ evidence of rapid, vertical, irreversible transport of lower tropospheric air into the lower tropical stratosphere by convective cloud turrets and by larger-scale upwelling in tropical cyclones, J. Geophys. Res. 98, 8665 - 8681

Ellis, T., T L'Ecuyer, J M. Haynes, and G L. Stephens, 2008; How often does it rain over the global oceans? The perspective from CloudSat , submitted to Geophys. Res. Lett

Gettelman, A., M. L. Salby, and F. Sassi, 2002: Distribution and influence of convection in the tropical tropopause region, J. Geophys. Res., 107(D10), 4080, doi:10.1029/2001JD001048

Haladay, T. and G. L Stephens, 2008; Characteristics of Tropical Thin Cirrus Clouds Deduced from Joint CloudSat and CALIPSO Observations, submitted to J. Geophys. Res.

Haynes, J. M., and G. L. Stephens (2007), Tropical oceanic cloudiness and the incidence of precipitation: Early results from CloudSat, Geophys. Res. Lett., 34, L09811, doi:10.1029/2007GL029335.

Haynes, J., R. T. Marchand, Z. Luo, A. Bodas-Salcedo, and G. L. Stephens, 2007; A Multipurpose Radar Simulation Package: QuickBeam, Bull. Amer. Met. Soc., 88, pp. 1723–1727

Haynes, J., T. L'Ecuyer, G. Stephens, S. Miller, C Mitrescu and S. Tanelli, 2008; Rainfall retrieval over the ocean with spaceborne W-band radar, J. Geophys. Res. In press.

Kuang, Z. and C. S. Bretherton, 2004: Convective influences on the heat budget of the tropical tropopause layer: A cloud-resolving model study, J. Atmos. Sci. 61, 2919 – 2927

Lebsock M, G. L Stephens, amd C Kummerow, 2008; Multi-Sensor Observations of Aerosol Effects on Warm Clouds, J. Geophys. Res., in press.

L'Ecuyer, T,N. Wood., T. Haladay, G. Stephens and E Eloranta, 2008; Assessing The impact of clouds on the atmospheric radiation budget assessed with the CloudSat Fluxes and Heating rate product, to appear J. Geophys. Res.,

Liu, C. and E. J. Zipser, 2005: Global distributon of convection penetrating the tropical tropopause, J. Geophys. Res., 110, D23104, doi:10.1029/2005JD006063

Luo, Z., G. Liu and G. L. Stephens, CloudSat Adding New Insight into Tropical Penetrating Convection, Geophys. Res. Lett. In press

Mace, G. G., R. Marchand, Q. Zhang, and G. L. Stephens (2007), Global hydrometeor occurrence as observed by CloudSat: Initial observations from summer 2006, Geophys. Res. Lett., 34, L09808, doi:10.1029/2006GL029017.

Mace. G., Q. Zhang, M. Vaughan, R. Marchand, G. Stephens, C. Trepte, D. Winker, 2008: A Description of Hydrometeor Layer Occurrence Statistics Derived from the First Year of Merged Cloudsat and CALIPSO Data, to appear J. Geophys. Res.

Petty, G. W. (1997), An inter-comparison of oceanic precipitation frequencies from 10 special sensor microwave/imager rain rate algorithms and shipboard present weather reports, J. Geophys. Res., 102(D2), 1757–1777.

Rossow, W. B., and C. Pearl, 2007: 22-year survey of tropical convection penetrating into the lower stratosphere, Geophys. Res. Lett., 34, L04803, doi:10.1029/2006GL028635

Satoh, M., T. Matsuno, H. Tomita, H. Miura, T. Nasuno, and S. Iga (2008), Nonhydrostatic Icosahedral Atmospheric Model (NICAM) for global cloud resolving simulations, J. Comp. Phys., 227, 3486--3514, doi:10.1016/j.jcp.2007.02.006

Sherwood, C. S., T. Horinouchi and H. A. Zeleznik, 2003: Convective impact on 317 temperatures observed near the tropical tropopause. J. Atmos. Sci., 60, 1847 – 1856.

Sherwood, C. S. and A. E. Dessler, 2000: On the control of stratospheric humidity, 319 Geophys. Res. Lett., 27, 2513 – 2516

Stephens, G. L., 1978: Radiation profiles in extended water clouds: II. Parameterization schemes. J. Atmos. Sci., 35, 2123-2132.

Stephens, G.L and C. Kummerow, 2007; The remote sensing of clouds and precipitation from space: A review. J. Atmos. Sci., 64, 3742–3765.

Stephens, G.L and J. Haynes, 2007: Near Global Observations of the Warm Rain Auto-conversion Process. Geophys. Res. Lett., 34, L20805, doi:10.1029/2007GL030259

Stephens, G. L., and T. D. Ellis, 2008: Global-scale controls of precipitation efficiency in global warming GCM experiments. J. Clim. In press

Stephens, G.L et al., 2008, The CloudSat Mission: Performance and early science after the first year of operation, J. Geophys. Res. in press

Stephens, G. L., et al. (2002), The CloudSat mission and the A-Train, Bull. Am. Meteorol. Soc., 83, 1771--1790.

Suzuki, K and G.L Stephens, 2008a; On the relationship between radar reflectivity and the time scale of warm rain formation in a global cloud resolving model, submitted to J. Geophys. Res

Suzuki, K and G.L Stephens, 2008b; Global identification of warm cloud microphysical 1 processes with combined use of A-Train observations, Geophys. Res Lett, 35, L08805, doi:10.1029/2008GL033590.

Su, H., J.H. Jiang, D.V. Vane and G.L. Stephens, 2008; Vertical Structure of Tropical Clouds Sorted in Large-scale Regimes, submitted to Geophys. Res. Lett.

Twomey, S., 1977; The influence of pollution on the shortwave albedo of clouds, J. Atmos.Sci., 34, 149-1152.

Waliser et al., 2008 Cloud Ice: A Climate Model Challenge With Signs and Expectations of Progress, submitted to: J. Geophys Res.

Wang, J., W. B. Rossow, Y. Zhang, 2000: Cloud vertical structure and its variations from a 20-Yr global rawinsonde dataset. J. Climate, 13, 3041-3056.

Warren, S. G., C. J. Hahn, J. London,, R. M. Chervin, and R. L. Jenne, 1986: Global distribution of total cloud cover and cloud type amounts over land. NCAR Tech. Note TN-273 1STR, Boulder, CO, 29 pp. and 200 maps.

Wyant, M. C., C. S. Bretherton, J. T. Bacmeister, J. T. Kiehl, I. M. Held, M. Zhao, S. A. Klein, and B. A. Soden (2006), A comparison of low-latitude cloud properties and their response to climate change in three AGCMs sorted into regimes using mid-tropospheric vertical velocity, Clim. Dyn., 27, 261-279.